

Seismic elastic RTM with vector-wavefield decomposition

Ying Shi^{1,2}, Wei Zhang¹ and Yanghua Wang^{1,2,*} 

¹ Northeast Petroleum University, School of Earth Science, Daqing City, Heilongjiang Province, 163318, China

² Centre for Reservoir Geophysics, Department of Earth Science and Engineering, Imperial College London, South Kensington, London, SW7 2BP, UK

*Corresponding author: Yanghua Wang. E-mail: yanghua.wang@imperial.ac.uk

Received 28 December 2018, revised 5 February 2019

Accepted for publication 30 March 2019

Abstract

The advanced seismic imaging technology is reverse-time migration (RTM), which generates Earth's structural image by cross-correlating the forward-propagated source wavefield and the back-propagated receiver wavefield. Both these wavefields conventionally are assumed to be acoustic waves. When applying this RTM technology to seismic elastic waves, which are the multi-component rather than the single-component data, the cross-correlation procedure will suffer from a crosstalk effect between different wave modes. Therefore, prior to RTM imaging, both the source and receiver wavefields need to be decomposed into the pure P-wave mode and the pure S-wave mode. This paper envisages the advanced features of a vector-wavefield decomposition method that presents either the P- or the S-wave mode as a vector wavefield. This vector-wavefield decomposition method is based on a group of decoupled wave equations. The two separated vector wavefields preserve the true amplitude and phase information. Then, the associated RTM imaging condition is an inner-product of these two vector wavefields, rather than the cross correlation that is applicable to two scalar wavefields. The conventional elastic RTM approach uses the Helmholtz decomposition method to derive P- and S-waves and then implements cross correlation to produce the image. In comparison to this conventional combination, this paper demonstrates that the elastic RTM method using a combination of the vector-wavefield decomposition and the inner-product imaging condition is capable of producing seismic images with correct amplitudes and phases of various reflection modes.

Keywords: elastic RTM, Helmholtz decomposition, imaging condition, reverse-time migration, vector-wavefield decomposition

1. Introduction

In the seismic imaging process, an advanced technology called reverse-time migration (RTM) accomplishes seismic data repositioning (migration) by exploiting the correlation feature between forward-propagation wavefields initiated from the sources and back-propagation (reverse-time) wavefields originating from the receivers (Baysal *et al.* 1983). When the RTM technology is applied conventionally to seismic data and recoded by a single component, the wavefield simulation procedure uses the acoustic wave equation. Thus, it is referred to as an acoustic RTM (McMechan 1983). When the RTM technology is applied to seismic multi-component data, the wavefield simulation procedure uses the elastic-wave equation. It is referred to as an elastic RTM (Chang & McMechan, 1987, 1994; Sun & McMechan 2001; Symes 2007; Wang & McMechan 2015; Yong *et al.* 2016).

The elastic RTM technology may enhance ray illumination over a subsurface's structure and provide an accurate image of that structure. This is because the multi-component seismic data contain complete subsurface information. For instance, when encountering a gas cloud, the P-wave is weak, but the elastic RTM technology appears to be effective in imaging. The development of the elastic-wave migration has been through stages including Kirchhoff elastic-wave migration and one-way wave-equation migration (Dai & Kuo 1986; Wu 1994; Hokstad 2000; Xie & Wu 2005; Wang & Liu 2017), prior to the current elastic RTM stage. Elastic RTM technology uses a two-way elastic-wave equation for wavefield simulation and exhibits great superiority in handling complex velocity models, especially for steeply dipping structures, if compared to previous versions of elastic-wave migration methods.

Once an accurate source wavefield and an accurate receiver wavefield are obtained, we match these two types of wavefields to produce a subsurface image in which matched points represent the individual scatters or groups of aligned scatters. Various matching methods in RTM processing are various imaging conditions (Claerbout 1971). The performance of the imaging condition directly affects the quality of the migration profile, such as the amplitude recovery and the noise level in final RTM images. In any case, both the source and receiver wavefields need to be decomposed into the P- and the S-mode wave prior to the application of the imaging condition in order to avoid any potential crosstalk effect among different mode waves.

A conventional wave separation method is the Helmholtz decomposition method, based on the divergence calculation and the curl operation over a coupled elastic wavefield. This method produces two scalar wavefields, the P- and S-wavefields, which have incorrect amplitudes and incorrect phases. In this paper, we envisage a vector-wavefield decomposition method that separates both the source and receiver wavefields into vector wavefields, rather than scalar wavefields. This method is based on a group of decoupled wave equations, which produce the P- and S-waves with accurate amplitudes and correct phase characteristics.

A conventional imaging condition is to cross-correlate two wavefields. The P- and S-waves derived by the Helmholtz decomposition method are scalar, thus the RTM imaging condition is cross correlation (Xiao & Leaney 2010; Gu et al. 2015). However, once the source and receiver wavefields are decomposed, using the group of decoupled wave equations, into the two vector wavefields, an inner-product of two vector wavefields should be adopted as the imaging condition, to produce the RTM images of four modes effectively: PP, PS, SP and SS. This paper demonstrates that the combination of vector-wavefield decomposition and inner-product imaging condition is capable of producing RTM images with correct amplitudes and phases of different reflection modes.

2. A group of decoupled wave equations

For a seismic wave simulation in the elastic RTM, the two-dimensional (2D) elastic-wave equation can be presented in terms of particle-velocity and stress, as follows (Hall & Wang 2009):

$$\begin{aligned}\frac{\partial \tau_{xx}}{\partial t} &= (\lambda + 2\mu) \frac{\partial v_x}{\partial x} + \lambda \frac{\partial v_z}{\partial z}, \\ \frac{\partial \tau_{zz}}{\partial t} &= (\lambda + 2\mu) \frac{\partial v_z}{\partial z} + \lambda \frac{\partial v_x}{\partial x}, \\ \frac{\partial \tau_{xz}}{\partial t} &= \mu \left(\frac{\partial v_z}{\partial x} + \frac{\partial v_x}{\partial z} \right), \\ \rho \frac{\partial v_x}{\partial t} &= \frac{\partial \tau_{xx}}{\partial x} + \frac{\partial \tau_{xz}}{\partial z}, \\ \rho \frac{\partial v_z}{\partial t} &= \frac{\partial \tau_{zz}}{\partial z} + \frac{\partial \tau_{xz}}{\partial x},\end{aligned}\tag{1}$$

where (x, z) is the 2D spatial coordinates, (v_x, v_z) is the particle-velocity vector, τ_{xx} and τ_{zz} are the two normal stresses, τ_{xz} is the shear stress, ρ is the bulk density, (λ, μ) are Lamé constants and t is the travel time.

In either the source wavefield or the receiver wavefield, simulated using equation (1), the P- and S-mode waves are coupled. These coupled wavefields will unavoidably induce a crosstalk artifact in the final RTM images. Therefore, before the RTM imaging, both the source wavefield and the receiver wavefield need to be decomposed into the P- and S-mode waves.

A vector-wavefield decomposition method uses a group of decoupled wave equations (Wang et al. 2015). If taking out the time derivative of normal stress from the two time-derivatives (the first two expressions in equation (1)), the group of decoupled wave equations may be presented as

$$\begin{aligned} \frac{\partial \tau^p}{\partial t} &= (\lambda + 2\mu) \left(\frac{\partial v_x}{\partial x} + \frac{\partial v_z}{\partial z} \right), \\ \frac{\partial v_x^p}{\partial t} &= \frac{1}{\rho} \frac{\partial \tau^p}{\partial x}, \\ \frac{\partial v_z^p}{\partial t} &= \frac{1}{\rho} \frac{\partial \tau^p}{\partial z}, \\ v_x^s &= v_x - v_x^p, \\ v_z^s &= v_z - v_z^p, \end{aligned} \tag{2}$$

where τ^p is an auxiliary stress of the P-wave, (v_x^p, v_z^p) is the particle-velocity vector of the P-wave and (v_x^s, v_z^s) is the particle-velocity vector of the S-wave. The auxiliary P-wave stress τ^p is a scalar, similar to the pressure of the acoustic wave, rather than a vector. The first expression in equation (2) indicates that the scalar τ^p is calculated based on (v_x, v_z) the particle-velocity components of the full wavefield. The second and third expressions indicate that the particle-velocity wavefield of the P-wave (v_x^p, v_z^p) is calculated using τ^p , the P-wave stress. Then, the other two expressions indicate that the particle-velocity wavefield of the S-wave (v_x^s, v_z^s) is calculated from (v_x, v_z) , the particle-velocity components of the full wavefield. Therefore, equation (2) is referred to as a group of decoupled wave equations.

Equations (1) and (2) are solved numerically by using a staggered-grid finite difference approach (Virieux 1986). Equation (1) is written in the discrete expression as

$$\begin{aligned} [\tau_{xx}]_{i+1/2,j}^{k+1} &= [\tau_{xx}]_{i+1/2,j}^k + \Delta t [(\lambda + 2\mu) D_x [v_x]_{ij}^{k+1/2} + \lambda D_z [v_z]_{i+1/2,j+1/2}^{k+1/2}], \\ [\tau_{zz}]_{i+1/2,j}^{k+1} &= [\tau_{zz}]_{i+1/2,j}^k + \Delta t [(\lambda + 2\mu) D_z [v_z]_{i+1/2,j+1/2}^{k+1/2} + \lambda D_x [v_x]_{ij}^{k+1/2}], \\ [\tau_{xz}]_{ij+1/2}^{k+1} &= [\tau_{xz}]_{ij+1/2}^k + \Delta t [\mu D_z [v_x]_{ij}^{k+1/2} + \mu D_x [v_z]_{i+1/2,j+1/2}^{k+1/2}], \\ [v_x]_{ij}^{k+1/2} &= [v_x]_{ij}^{k-1/2} + \frac{\Delta t}{\rho} (D_x [\tau_{xx}]_{i+1/2,j}^k + D_z [\tau_{xz}]_{ij+1/2}^k), \\ [v_z]_{i+1/2,j+1/2}^{k+1/2} &= [v_z]_{i+1/2,j+1/2}^{k-1/2} + \frac{\Delta t}{\rho} (D_z [\tau_{zz}]_{i+1/2,j}^k + D_x [\tau_{xz}]_{ij+1/2}^k). \end{aligned} \tag{3}$$

Equation (2) is also written in the discrete expression as

$$\begin{aligned} [\tau_{pp}]_{i+1/2,j}^{k+1} &= [\tau_{pp}]_{i+1/2,j}^k + \Delta t [(\lambda + 2\mu) (D_x [v_x]_{ij}^{k+1/2} + D_z [v_z]_{i+1/2,j+1/2}^{k+1/2})], \\ [v_x^p]_{ij}^{k+1/2} &= [v_x^p]_{ij}^{k-1/2} + \frac{\Delta t}{\rho} D_x [\tau_{pp}]_{i+1/2,j}^k, \\ [v_z^p]_{i+1/2,j+1/2}^{k+1/2} &= [v_z^p]_{i+1/2,j+1/2}^{k-1/2} + \frac{\Delta t}{\rho} D_z [\tau_{pp}]_{i+1/2,j}^k, \\ [v_x^s]_{ij}^{k+1/2} &= [v_x]_{ij}^{k+1/2} - [v_x^p]_{ij}^{k+1/2}, \\ [v_z^s]_{i+1/2,j+1/2}^{k+1/2} &= [v_z]_{i+1/2,j+1/2}^{k+1/2} - [v_z^p]_{i+1/2,j+1/2}^{k+1/2}. \end{aligned} \tag{4}$$

The two operators D_x and D_z in the discrete equation (3) and equation (4) are the high-order finite-differencing operators for first-order spatial differentials,

$$D_x f_{ij}^k = \frac{1}{\Delta x} \sum_{n=1}^N C_n^N (f_{i+n-1/2,j}^k - f_{i-n+1/2,j}^k),$$

$$D_z f_{ij}^k = \frac{1}{\Delta z} \sum_{n=1}^N C_n^N (f_{ij+n-1/2}^k - f_{ij-n+1/2}^k),$$

$$C_n^N = \frac{(-1)^{n+1}}{2n-1} \prod_{i=1, i \neq n}^N (2i-1)^2 \times \left(\prod_{i=1}^{n-1} [(2n-1)^2 - (2i-1)^2] \right)^{-1} \left(\prod_{j=n+1}^N [(2j-1)^2 - (2n-1)^2] \right)^{-1}. \quad (5)$$

3. The effectiveness of the vector-wavefield decomposition method

In this section, the vector-wavefield decomposition method described in the previous section is compared with another wavefield decomposition method, the Helmholtz decomposition method (Aki & Richards 1980; Dellinger & Etgen 1990; Sun et al. 2004; Yan & Sava 2008; Sun et al. 2011; Du et al., 2012, 2014). In the Helmholtz decomposition method, the P-wavefield is extracted by the divergence operation on the elastic wavefield, and the S-wavefield is extracted by the curl operation on the elastic wavefield.

These two wavefield decomposition methods are applied to multi-component seismic data, generated from a homogeneous isotropic elastic model. The P- and S-velocities and the density are all at a constant, $V_p = 3000 \text{ m s}^{-1}$, $V_s = V_p/\sqrt{3}$, $\rho = 2000 \text{ kg m}^{-3}$. A source signature is defined by a Ricker wavelet with a 25-Hz peak frequency (Wang 2015a, 2015b), and the source wavelet is put on the vertical component of the particle-velocity vector, v_z , at position (0, 0) in the homogeneous model. In this way, the ‘source’ can generate the source signature of P-mode and S-mode simultaneously for the purpose of demonstrating wavefield decompositions. The model size is 200×200 grids with a cell size of 10 m. The time sampling rate of seismic traces is 1 ms.

Figures 1 and 2 display snapshots of the elastic wavefield at the time of 710 ms. In both figures, the positive amplitudes are presented in red and the negative amplitudes are presented in blue. Meanwhile, figure 3 compares the waveforms directly taken along the dotted line annotated in figure 1a. These comparisons confirm that the vector-wavefield decomposition method has a prominent advantage over the Helmholtz decomposition method, and that the vector-wavefield decomposition method preserves both the phase and amplitude characteristics.

From these three figures, we made the following observations.

- (1) The P- and the S-waves are coupled in both the horizontal component v_x (figures 1a and 3a) and the vertical component v_z (figures 1b and 3b) of the particle-velocity wavefield.
- (2) Using the Helmholtz decomposition method, the separated P-wave is obtained by the divergence operation (figure 1c and figure 3c), and the separated S-wave is obtained by the curl operation of the particle-velocity wavefield (figure 1d and figure 3d).
- (3) The Helmholtz decomposition method has changed the amplitude information and induced a 90° phase rotation from the original elastic wavefield (Sun et al. 2001, 2004), if we compare figure 1c and 1d (figures 3c and 3d) with the images appeared in figure 1a and 1b (figures 3a and 3b).
- (4) Using the vector-wavefield decomposition method, the P-wave can be separated cleanly from the S-wave in either components. The P-wave vector consists of figure 2a and 2c (or figures 3e and 3g), and the S-wave vector consists of figure 2b and d (or figures 3f and 3h).

In the Helmholtz decomposition method, the separated P-wave is a scalar, but the separated S-wave, obtained from the curl operation, is a vector. This derived S-wave vector in the 2D case has only the y -component, because in the curl operation, $\nabla \times [v_x, v_y, v_z]^T$, the only possible nonzero component is $u_y \equiv \partial v_x / \partial z - \partial v_z / \partial x \neq 0$. This y -component can be considered as a scalar in the imaging process, which will be discussed in the following section.

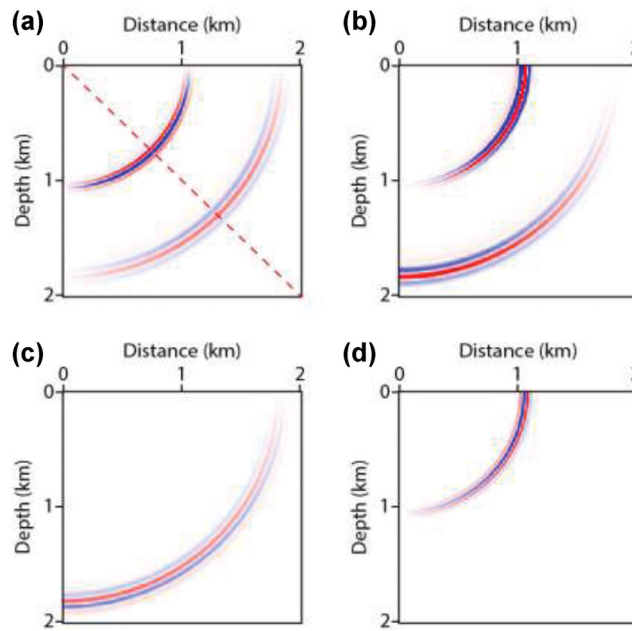


Figure 1. The Helmholtz decomposition method. (a) The horizontal component v_x of the particle-velocity wavefield. (b) The vertical component v_z of the particle-velocity wavefield. (c) P-wave, derived by the divergence calculation on the particle-velocity wavefield. (d) S-wave (y-component), obtained by the curl operation on the particle-velocity wavefield. Wavefield snapshots are taken at the time of 710 ms.

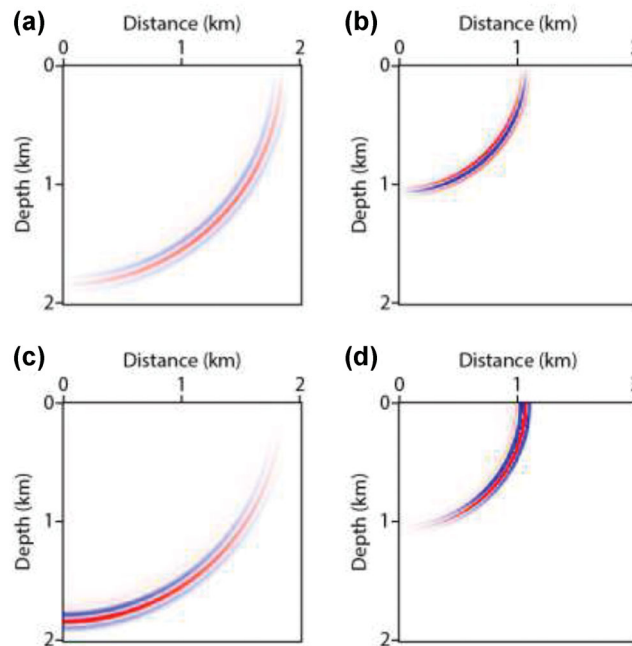


Figure 2. The vector-wavefield decomposition method. (a, b) The horizontal component of the P-mode wave and the S-mode wave. (c, d) The vertical component of the P-mode wave and S-mode wave. Wavefield snapshots are taken at the time of 710 ms.

In the Helmholtz decomposition method, the amplitude inaccuracy and phase rotation in the derived P- and S-waves require additional corrections. For correcting the amplitude ratio between the P-wave and the S-wave, it needs additional knowledge of the particle velocities of these two wave modes (Sun *et al.* 2011; Nguyen & McMechan 2015). The 90°-phase rotation needs also to be corrected or, otherwise, the polarity reversal would badly deteriorate the PS or SP images. The correction of the 90°-phase rotation can easily be achieved through Hilbert transform (Sun *et al.* 2001). Note that these amplitude and phase corrections not only involve additional computation but also introduce potential artifacts (Wang *et al.* 2015).

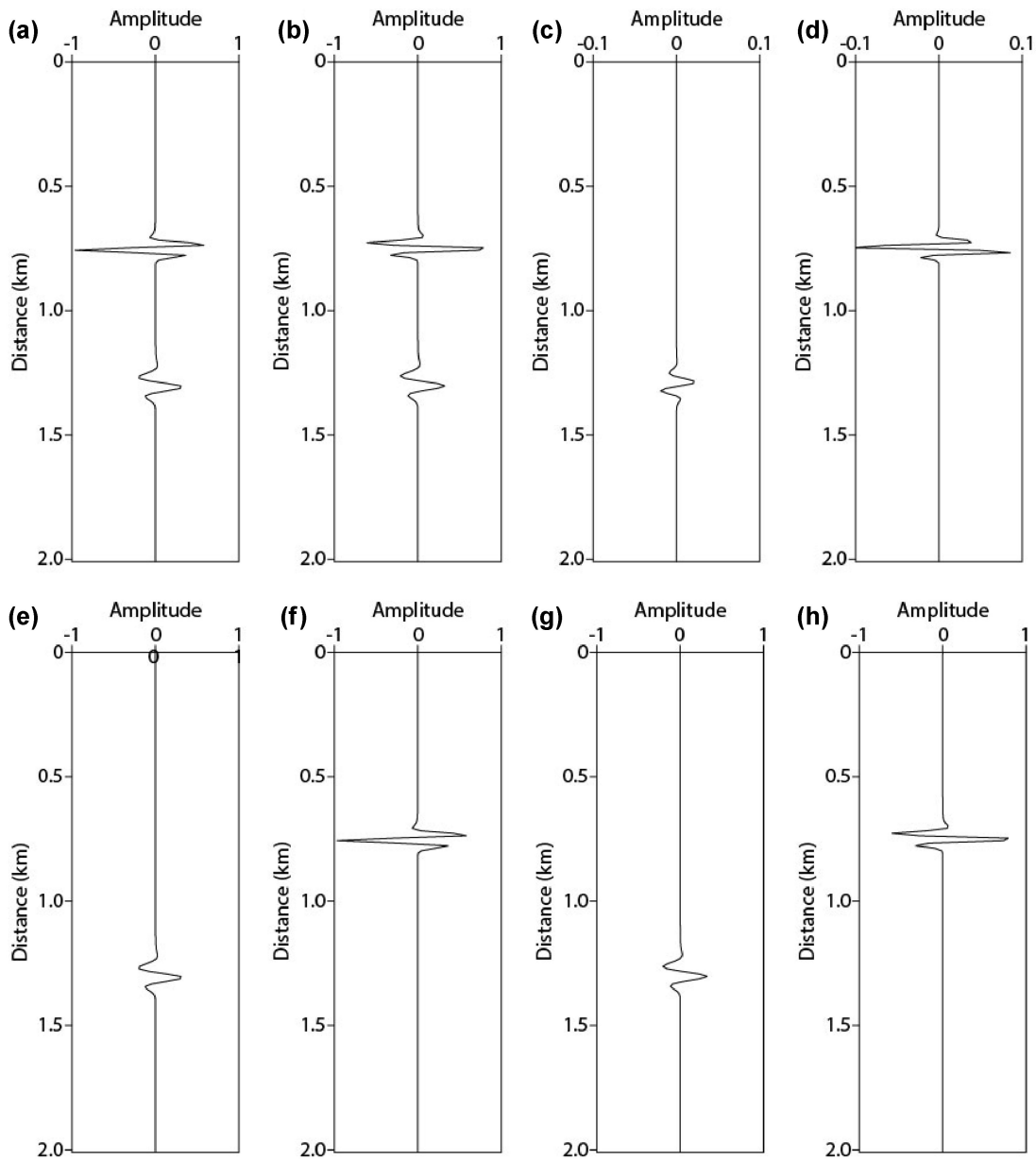


Figure 3. Waveform comparison of the snapshots in figure 1 and figure 2 (along the dotted line shown in figure 1a). The Helmholtz decomposition method (parts c and d corresponding to figure 1c and d, respectively) has changed the phase and amplitude change. The vector-wavefield decomposition method (parts e, f, g and h corresponding to figure 2a, b, c and d, respectively) preserves both the phase and the amplitude.

In contrast, vector-wavefield decomposition using the group of decoupled wave equations (figure 2 or figure 3e–h) preserves both the phase and amplitude information of the input vector wavefield. Thus, there is no additional correction either for the amplitude or the phase, and there is no polarity-reversal issue that exists in the Helmholtz decomposition method.

4. RTM imaging conditions

The imaging condition is critical to the RTM results. When applied to the P- and S-waves derived by the Helmholtz decomposition method, the following cross-correlation imaging condition is used:

$$I_{ij}(x, z) = \frac{\sum_t S_i(t; x, z) R_j(t; x, z)}{\sum_t S_i^2(t; x, z)}, \quad (6)$$

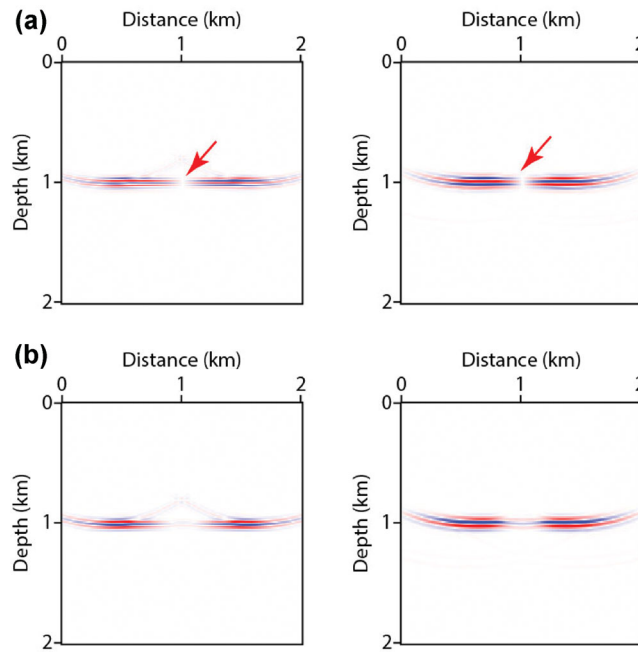


Figure 4. The RTM images generated using two different combinations. (a) PS and SP images, generated by the conventional combination of the Helmholtz decomposition method and the cross-correlation imaging condition. These images reveal the polarity-reversal issue (arrows). (b) PS and SP images, generated by the combination of the vector-wavefield decomposition method and the inner-product imaging condition, do not have the polarity-reversal issue.

where i and j denote the wave either in the P- or S-mode, S_i is the i -mode wave derived from the source wavefield and R_j is the j -mode wave derived from the receiver wavefield. In this case, the P-wave derived from the divergence calculation is a scalar, and the S-wave derived from the curl operation is a vector though. Thus, it is necessary to derive a scalar representation for the S-wave (Du et al., 2014, 2017). For the derived S-wave in the 2D case, the y -component that is orthogonal to x and z components can be considered a scalar and is applicable to the cross correlation (6).

For the separated waves obtained from the vector-wavefield decomposition method, the inner-product imaging condition should be used:

$$I_{ij}(x, z) = \frac{\sum_t \vec{S}_i(t; x, z) \cdot \vec{R}_j(t; x, z)}{\sum_t \|\vec{S}_i(t; x, z)\|^2}, \tag{7}$$

where \vec{S} is a vector wavefield derived from the source wavefield, \vec{R} is a vector wavefield derived from the receiver wavefield and ‘ \cdot ’ denotes the inner product of two vector wavefields.

In both equations (6) and (7), the cross correlation and the inner product are normalized using the wave energy of the source wavefield. This normalization process compensates for the source illumination.

Let us demonstrate these two imaging conditions using a two-layer model. The P-wave velocities of the two layers are $V_p = 2800$ and 3000 m s^{-1} , respectively. The S-wave velocities of the two layers are defined by the relation: $V_s = V_p / \sqrt{3}$. The density of the model is a constant of 2000 kg m^{-3} . The model size, cell size and time sampling rate are the same as the previous model. We put a source signature of the 20-Hz Ricker wavelet on both the normal stress components τ_{xx} and τ_{zz} , to mimic an explosive P-wave source. We generate the multi-component data with a 10-m receiver interval laterally.

We simulate only one shot gather at (1, 0) km, for this demonstration. Figure 4a illustrates the PS and SP images produced by the conventional combination of the Helmholtz decomposition method and cross-correlation imaging condition. Figure 4b illustrates the PS and SP images produced by the combination of the vector-wavefield decomposition method and inner-product imaging condition. Note that PS and SP in figure 4 do not stand for either the P-to-S or S-to-P-mode

conversion. The PS image is generated by the PP-mode transmission wavefield and the PS-mode reflection wavefield, and the SP image is generated by the PS-mode transmission wavefield and the PP-mode reflection wavefield.

The PS and SP images in figure 4a clearly evidence the polarity reversal, and arrows indicate the location where the polarity reversal occurred. This is because the S-mode wave derived by the curl operation has a polarity-reversal issue (Du *et al.* 2012; Gu *et al.* 2015). The latter does not cause destructive interference in the SS image though, generated by the PS-mode transmission wave and the PS-mode reflection wave derived from the source wavefield and the receiver wavefield, respectively. It is because the cross correlation between the two S-waves automatically compensates for the polarity reversal. In contrast, two images in figure 4b clearly do not have the issue of polarity reversal.

There are some methods to correct polarity reversal (Balch & Erdemir 1994; Sun & McMechan, 2001; Zhang & McMechan, 2010, 2011; Yan & Xie 2012; Li *et al.* 2016). One simple method is multiplying the imaging value by -1 at the positive (or negative) offset if the subsurface reflector is assumed to be horizontal. This assumption is inconsistent with a complicated subsurface structure though. Another possible method is based on the sign factor calculated by the incident and reflection directions. This method might be inaccurate (Duan & Sava 2015), because these directions calculated by Poynting vector or polarization vector become invalid when multi-pathing is involved. Therefore, it is still a challenging task to produce high-quality P-S and S-P imaging from seismic multi-component data, if the wave separation is made based on the Helmholtz decomposition method.

For the vector wavefields, the cross-correlation imaging condition cannot be used. If it is used, it will produce the following eight images: $P_x P_x$, $P_z P_z$, $P_x S_x$, $P_z S_z$, $P_x S_z$, $S_x P_x$, $S_x S_x$ and $S_z S_z$. These images do not have clear physical meanings as they are not consistent with the reflection coefficients. When the inner-product imaging condition is used, it produces reflection images of four modes: PP, PS, SP and SS. For example, $I_{p,s}$ in equation (7) refers to the inner-product image generated by the P-wave vector ($i = P$) derived from the source wavefield and the S-wave vector ($j = S$) derived from the receiver wavefield.

5. Application strategy

A straightforward implementation for RTM needs to store the source wavefield (or the receiver wavefield) at all the time steps, prepared for the imaging process using either the cross correlation or, here, the inner production. This implementation requires huge data storage and is not practical for the elastic RTM of multi-component seismic data. For reducing data storage, there are some investigations for the acoustic RTM (Feng & Wang 2012; Tan & Huang 2014; Liu *et al.* 2015; Raknes & Weibull 2016; Shi & Wang 2016), but seldom for the elastic RTM (Nguyen & McMechan 2015; Yong *et al.* 2016). In this paper, we propose a strategy that reconstructs source wavefield during the imaging stage, which greatly reduces the storage requirement and makes the elastic RTM applicable to multi-component seismic data.

This strategy does not store the source wavefield at all time steps. It stores (1) only the full wavefield at the two maximum-time steps, and (2) the particle-velocity components at all time steps but within a small portion of the absorbing boundary zone. The absorbing boundary condition we adopted for attenuating the artificial reflections from numerical boundaries was the perfectly matched layer method (Berenger 1994). We achieved this storage saving by trading in the computational cost, as the source wavefield was inversely reconstructed, simultaneously, at the time when the receiver wavefield was propagating. Previously, we have used stored two-part wavefields in the inverse reconstruction of the source wavefield. This innovative algorithm makes the implementation of the elastic RTM plausible in practice.

Therefore, our implementation for the elastic RTM algorithm includes three steps:

- (1) Simulating the source wavefield, but only storing the full wavefield at the two maximum-time steps and the particle-velocity components in part of the model space.
- (2) Back-propagating the source and receiver wavefield simultaneously. The source wavefield back-propagation starts from the stored full wavefield at the two maximum-time steps, and the receiver wavefield back-propagation starts from the 'virtual source', the multi-component seismic data.
- (3) Applying an imaging condition; in this case, inner production.

For a demonstration, the Marmousi-2 model is adopted. The model size is 1700×400 grids with x and z interval of 10 m. Figure 5 displays the P-wave velocity V_p . The S-wave velocity, V_s , is defined by $V_s = V_p / \sqrt{3}$ and the density is set to be a constant 2000 kg m^{-3} .

An explosive source is defined with a 25-Hz Ricker wavelet. There are 170 shot gathers generated along the surface in total. The shot point interval is 100 m. The multi-component receivers are also placed on the surface. The lateral interval between consecutive receiver points is 10 m. The seismic recording length is 10 s, with a time sampling interval of 1 ms.

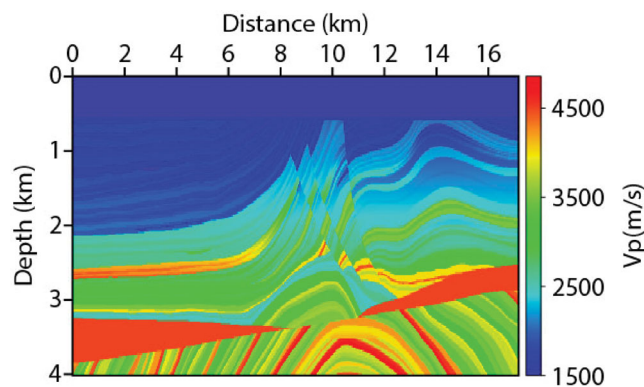


Figure 5. The P-wave velocity of the Marmousi-2 model.

Figures 6 and 7 compare the RTM results generated by two combinations. In figure 6, we use the conventional combination of the Helmholtz decomposition method and the cross-correlation imaging condition, while in figure 7, we use the combination of the vector-wavefield decomposition method and the inner-product imaging condition. We would like to clarify that the multi-component seismic data input to both figures 6 and 7 are identical and are generated by equation (1), although we use different methods for wavefield decomposition and, consequently, different imaging conditions.

We make the following observations.

- (1) PP and PS images from the RTM using vector wavefields are clearer and more continuous than those from the conventional method. All of structure features, such as the anticlines, faults and flat and dipping reflectors, are clearly and accurately presented. These reflection events are continuously imaged and positioned at the same depth in both the PP and PS images.
- (2) Both the PP and SS images generated by the two methods are very similar, except for the amplitude and phase. The reflections are continuous and have fewer artifacts compared to PS and SP images.
- (3) Using the combination of the vector-wavefield decomposition method and the inner-product imaging condition, there is no destructive interference on the PS and SP images.

Figure 8 displays snapshots (at the time of 1600 ms) of the source wavefield and the receiver wavefield. They are a sample shot gather, with the source positioned at (3, 0) km of the Marmousi-2 model. Both the source wavefield and receiver wavefield are cleanly separated using the vector-wavefield decomposition method, as displayed in Figure 9.

If a velocity model that is 10% higher than the true velocity model used in the vector-wavefield decomposition, as displayed in figure 10, there is the amplitude leakage of P- and S-mode waves into the opposite wave mode. For example, the S-wave snapshot (figure 10c and d) contains the residual of the P-wave amplitudes that should be in figure 10a and b. If this higher velocity model is used not only in wavefield decomposition but also in the simulation of source and receiver wavefields, as shown in Figure 11, the elastic RTM images have strongly deteriorated.

Although we have demonstrated the effectiveness of the combination of the vector-wavefield decomposition method and the inner-product imaging condition using synthetic seismic data, there is not yet any published example of a field seismic data application. However, there are few application examples of field seismic data using the conventional combination with further improvements. An improvement to the conventional combination is to employ the least-squares approach to refine the elastic RTM images through iterations with field data demonstrations. It can also be improved by applying a deblurring filter to the elastic RTM images within an iteration. This deblurring filter is designed to mitigate the crosstalk effect caused by multiparameter coupling (Feng *et al.* 2018). The field data examples include a three-component VSP data set (Ren *et al.* 2017), a crosswell data set (Feng & Schuster 2017), an OBC line of PP data that are treated as vertical components of the displacement vector (Duan *et al.* 2017) and a 2D line of marine seismic data that are treated as the negative average of the normal stress components (Feng *et al.* 2018). These examples all indicate that an elastic RTM method is sensitive to the accuracy of P-, S-wave velocities and density, as we demonstrated in figure 11. Therefore, a velocity-independent RTM algorithm might be the future developing direction.

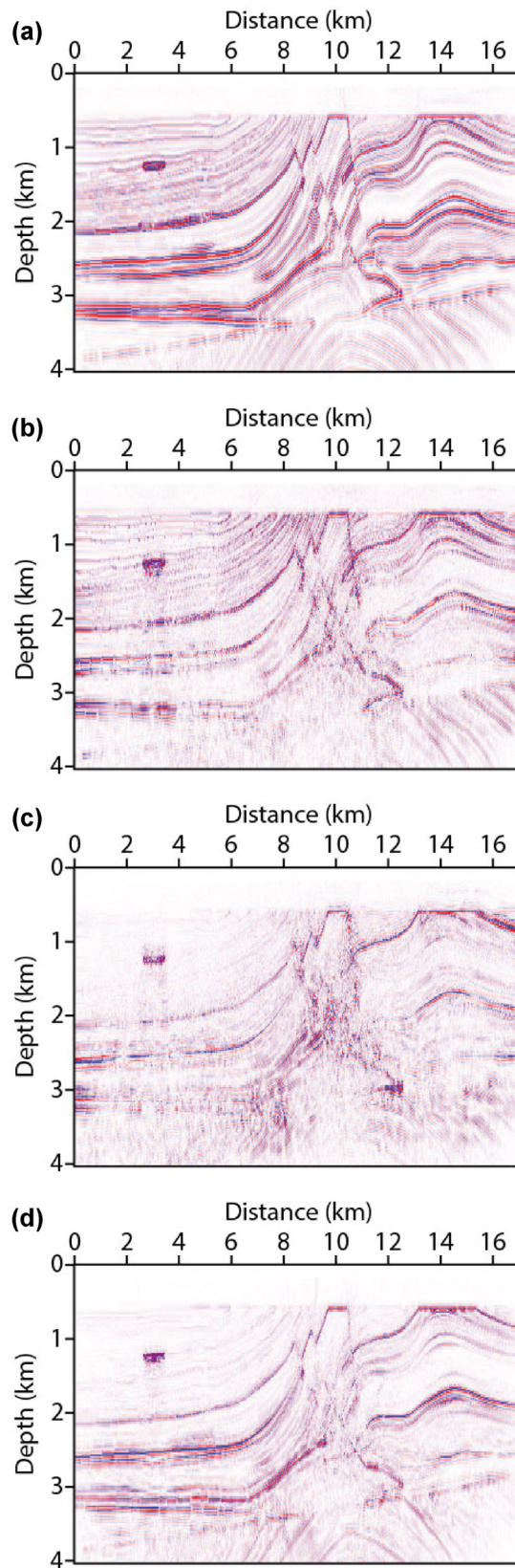


Figure 6. The elastic RTM result, using the conventional combination of the Helmholtz decomposition method and the cross-correlation imaging condition. (a–d) PP, PS, SP and SS images, respectively.

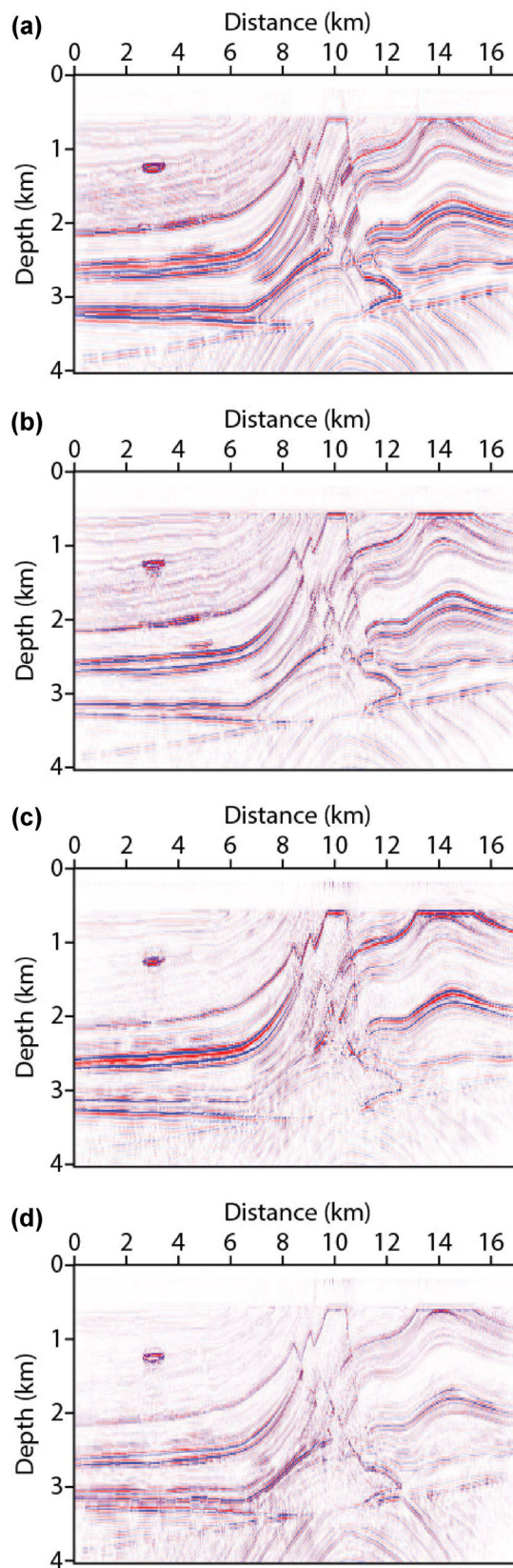


Figure 7. The elastic RTM result, using the combination of the vector-wavefield decomposition method and the inner-product imaging condition. (a–d) PP, PS, SP and SS images, respectively.

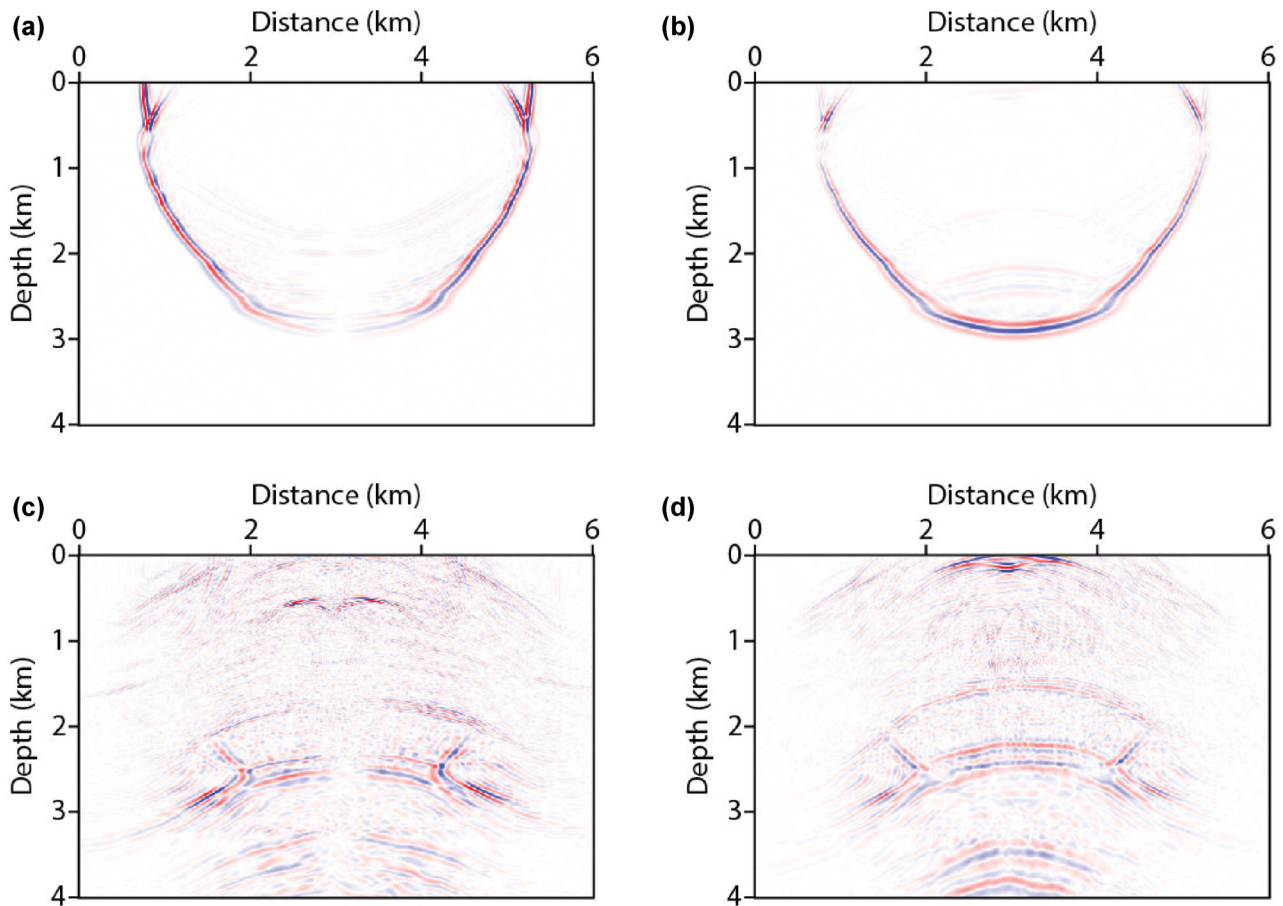


Figure 8. The snapshots of the source and receiver wavefields. (a, b) The horizontal and vertical components of the source wavefield. (c, d) The horizontal and vertical components of the receiver wavefield. The source is positioned at (3, 0) km of the Marmousi-2 model, and the wavefield snapshots are taken at the time of 1600 ms.

6. Conclusions

For the elastic RTM, which is applicable to multi-component seismic data, prior to the final imaging stage, the P- and S-waves need to be separated. We have compared two wavefield decomposition methods and, associated with these two methods, two imaging conditions. The first separation method is the Helmholtz decomposition method that derives the P-wave by the divergence calculation and the S-waves by the curl operation. The amplitude change and phase rotation in the separated waves may lead to destructive damage in the RTM images, and the PS and SP images show polarity reversal. The imaging condition is the conventional method of cross correlation between two scalar wavefields. The second method is the vector-wavefield decomposition method, based on decoupled wave equations. Separated P- and S-wavefields are vector wavefields that preserve both the amplitude and the phase characteristics. The associated imaging condition is the inner-product of these two vector wavefields. The final RTM images of various wave modes, including PP, PS, SP and SS reflections, present correct dynamic features.

Acknowledgements

The authors are grateful to the National Natural Science Foundation of China (Grant nos. 41574117), the Excellent Youth Foundation of Heilongjiang Province, China (Grant no. JJ2016JQ0036), and the sponsors of the Centre for Reservoir Geophysics, Imperial College London, for supporting this research.

Conflict of interest statement. None declared.

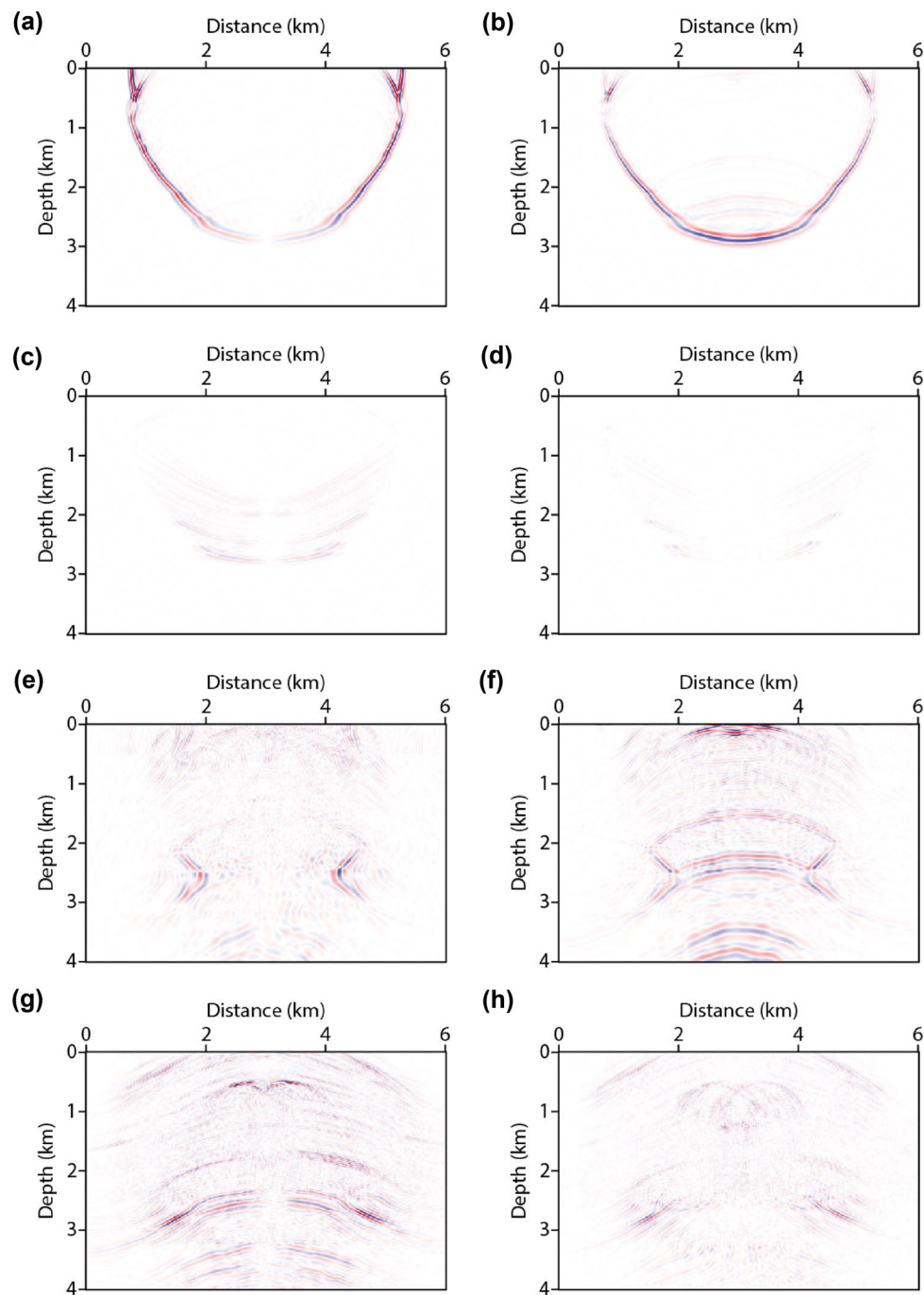


Figure 9. The vector-decomposed P- and S-waves. (a, b) The horizontal and vertical components of the P-mode wave decomposed from for the source wavefield. (c, d) The horizontal and vertical components of the S-mode wave decomposed for the source wavefield. (e, f) The horizontal and vertical components of the P-mode wave decomposed from the receiver wavefield. (g, h) The horizontal and vertical components of the S-mode wave decomposed for the receiver wavefield.

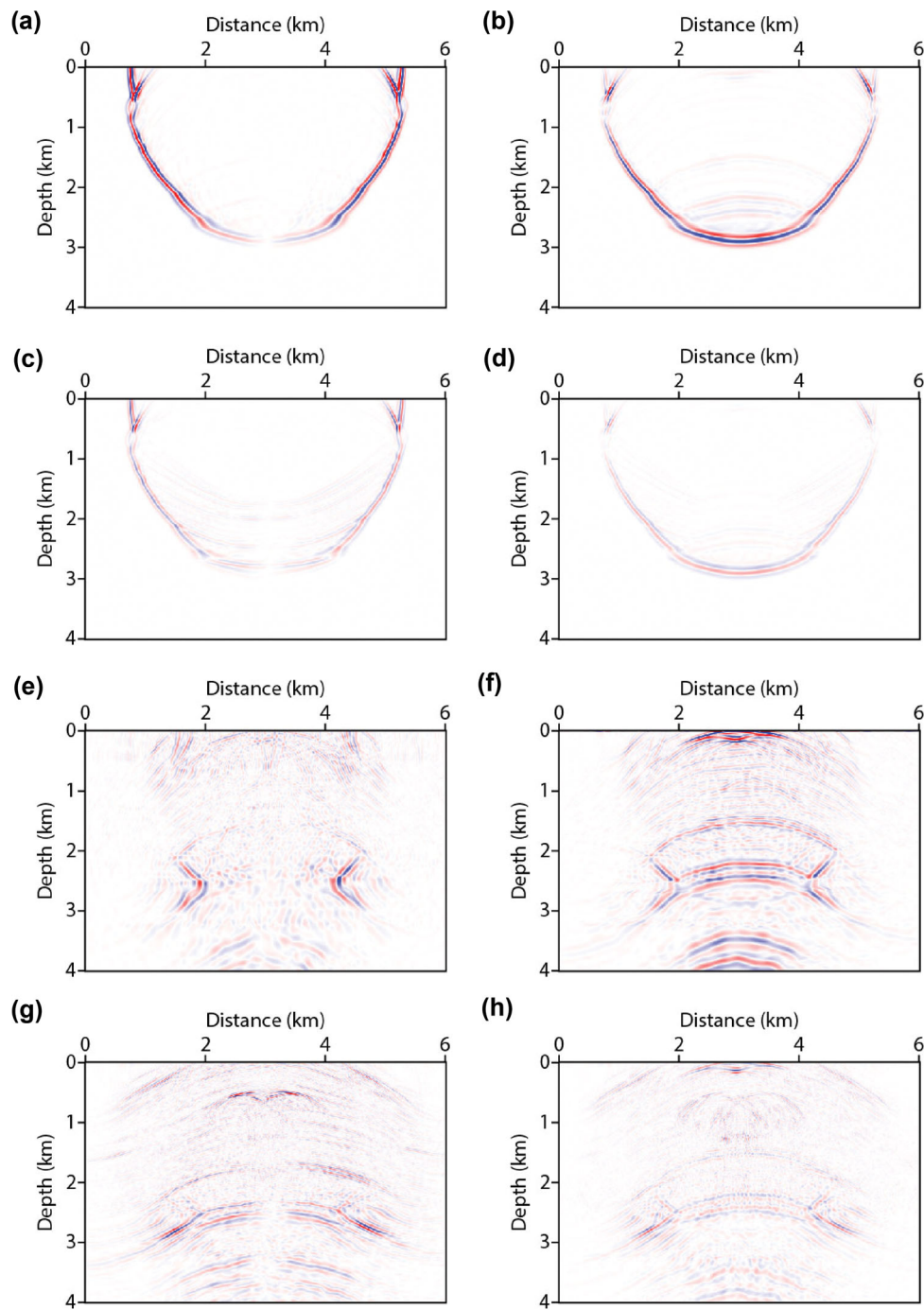


Figure 10. The vector-decomposed P- and S-waves using a velocity model that is 10% higher than the true model. (a, b) The horizontal and vertical components of the P-mode wave decomposed from the source wavefield. (c, d) The horizontal and vertical components of the S-mode wave decomposed for the source wavefield. (e, f) The horizontal and vertical components of the P-mode wave decomposed from the receiver wavefield. (g, h) The horizontal and vertical components of the S-mode wave decomposed for the receiver wavefield.

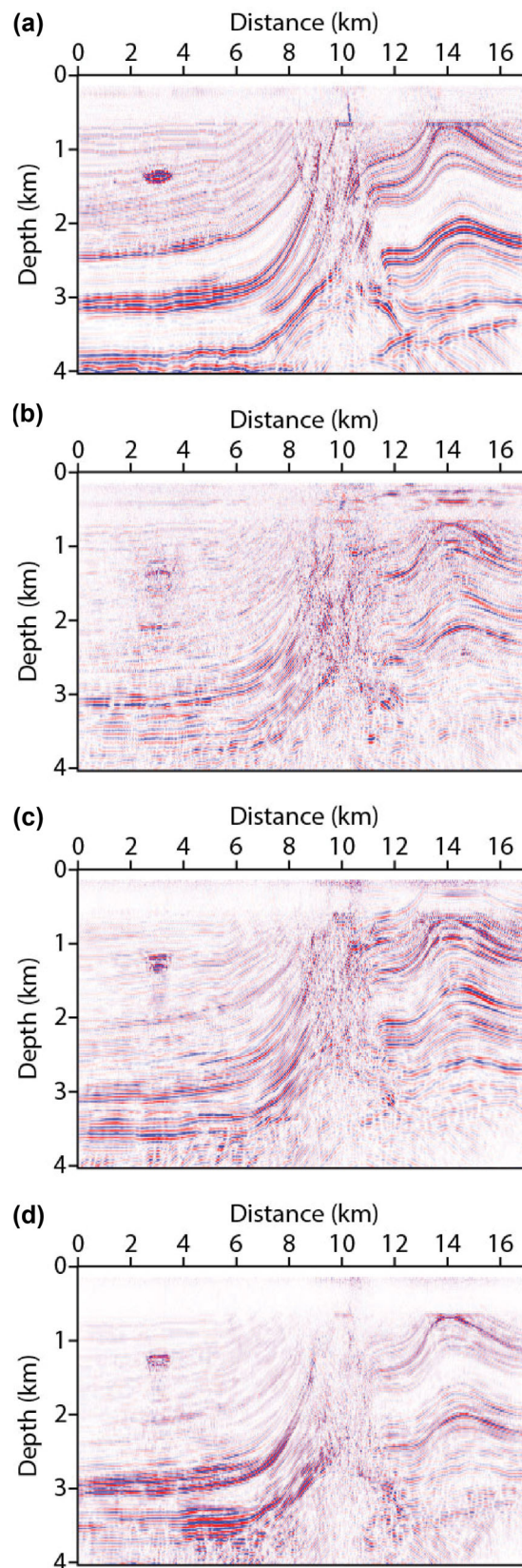


Figure 11. The elastic RTM images, using a velocity model that is 10% higher than the true Marmousi-2 model, and using the combination of the vector-wavefield decomposition method and the inner-product imaging condition. (a–d) PP, PS, SP and SS images, respectively.

References

- Aki, K. & Richards, P.G., 1980. *Quantitative Seismology: Theory and Methods*, Freeman, New York.
- Balch, A.H. & Erdemir, C., 1994. Sign-change correction for prestack migration of P-S converted wave reflections, *Geophysical Prospecting*, **42**, 637–663.
- Baysal, E., Kosloff, D. & Sherwood, J., 1983. Reverse time migration, *Geophysics*, **48**, 1514–1524.
- Berenger, J., 1994. A perfectly matched layer for the absorption of electromagnetic waves, *Journal of Computational Physics*, **114**, 185–200.
- Chang, W.F. & McMechan, G.A., 1987. Elastic reverse-time migration, *Geophysics*, **52**, 1365–1375.
- Chang, W.F. & McMechan, G.A., 1994. 3D elastic prestack reverse-time depth migration, *Geophysics*, **59**, 597–609.
- Claerbout, J.F., 1971. Toward a unified theory of reflector mapping, *Geophysics*, **36**, 467–481.
- Dai, T. & Kuo, J.T., 1986. Real data results of Kirchhoff elastic wave migration, *Geophysics*, **51**, 1006–1011.
- Dellinger, J. & Etgen, J., 1990. Wave-field separation in two-dimensional anisotropic media, *Geophysics*, **55**, 914–919.
- Du, Q., Gong, X., Zhang, M., Zhu, Y. & Fang, G., 2014. 3D PS-wave imaging with elastic reverse-time migration, *Geophysics*, **79**, S173–S184.
- Du, Q., Guo, C., Zhao, Q., Gong, X., Wang, C. & Li, X., 2017. Vector-based elastic reverse time migration based on scalar imaging condition, *Geophysics*, **82**, S111–S127.
- Du, Q., Zhu, Y. & Ba, J., 2012. Polarity reversal correction for elastic reverse time migration, *Geophysics*, **77**, S31–S41.
- Duan, Y. & Sava, P., 2015. Scalar imaging condition for elastic reverse time migration, *Geophysics*, **80**, S127–S136.
- Duan, Y., Guitton, A. & Sava, P., 2017. Elastic least-squares reverse time migration, *Geophysics*, **82**(4), S315–S325.
- Feng, B. & Wang, H., 2012. Reverse time migration with source wavefield reconstruction strategy, *Journal of Geophysics and Engineering*, **9**, 69–74.
- Feng, Z., Guo, B. & Schuster, G. T., 2018. Multiparameter deblurring filter and its application to elastic migration and inversion, *Geophysics*, **83**(5), S421–S435.
- Feng, Z. & Schuster, G. T., 2017. Elastic least-squares reverse time migration, *Geophysics*, **82**(2), S143–S157.
- Gu, B., Li, Z. & Ma, X., 2015. Multi-component elastic reverse time migration based on the P- and S-wave separated velocity-stress equations, *Journal of Applied Geophysics*, **112**, 62–78.
- Hall, F. & Wang, Y., 2009. Elastic wave modelling by an integrated finite difference method, *Geophysical Journal International*, **177**, 104–114.
- Hokstad, K., 2000. Multicomponent Kirchhoff migration, *Geophysics*, **65**, 861–873.
- Li, Z., Ma, X. & Liang, G., 2016. Wavefield separation and polarity reversal correction in elastic reverse time migration, *Journal of Applied Geophysics*, **127**, 56–67.
- Liu, S., Li, X., Wang, W. & Zhu, T., 2015. Source wavefield reconstruction using a linear combination of the boundary wavefield in reverse time migration, *Geophysics*, **80**, S203–S212.
- McMechan, G.A., 1983. Migration by extrapolation of time-dependent boundary values, *Geophysical Prospecting*, **31**, 413–420.
- Nguyen, B. & McMechan, G.A., 2015. Five ways to avoid storing source wavefield snapshots in 2D elastic prestack reverse-time migration, *Geophysics*, **80**, S1–S8.
- Raknes, E.B. & Weibull, W., 2016. Efficient 3D elastic full-waveform inversion using wavefield reconstruction methods, *Geophysics*, **81**, R45–R55.
- Ren, Z., Liu, Y. & Sen, M. K., 2017. Least-squares reverse time migration in elastic media, *Geophysical Journal International*, **208**, 1103–1125.
- Shi, Y. & Wang, Y., 2016. Reverse time migration of 3D vertical seismic profile data, *Geophysics*, **81**(1), S31–S38.
- Sun, R., Chow, J. & Chen, K., 2001. Phase correction in separating P- and S-waves in elastic data, *Geophysics*, **66**, 1515–1518.
- Sun, R. & McMechan, G.A., 2001. Scalar reverse-time depth migration of prestack elastic seismic data, *Geophysics*, **66**, 1519–1527.
- Sun, R., McMechan, G. A. & Chuang, H., 2011. Amplitude balancing in separating P- and S-waves in 2D and 3D elastic seismic data, *Geophysics*, **76**, S103–S113.
- Sun, R., McMechan, G. A., Hsiao, H.H. & Chow, J., 2004. Separating P and S-waves in prestack 3D elastic seismograms using divergence and curl, *Geophysics*, **69**, 286–297.
- Symes, W.W., 2007. Reverse time migration with optimal checkpointing, *Geophysics*, **72**, SM213–SM221.
- Tan, S. & Huang, L., 2014. Reducing the computer memory requirement for 3D RTM, *Geophysics*, **79**, S185–S194.
- Virieux, J., 1986. P-SV wave propagation in heterogeneous media: velocity-stress finite-difference method, *Geophysics*, **51**, 889–901.
- Wang, E. & Liu, Y., 2017. The hybrid absorbing boundary condition for one-step extrapolation and its application in wavefield decomposition-based reverse time migration, *Journal of Geophysics and Engineering*, **14**, 1177–1188.
- Wang, W. & McMechan, G.A., 2015. Vector-based elastic reverse time migration, *Geophysics*, **80**, S245–S258.
- Wang, W., McMechan, G.A. & Zhang, Q., 2015. Comparison of two algorithms for isotropic elastic P and S decomposition in the vector domain, *Geophysics*, **80**, T147–T160.
- Wang, Y., 2015a. Frequencies of the Ricker wavelet, *Geophysics*, **80**, A31–A37.
- Wang, Y., 2015b. The Ricker wavelet and the Lambert W function, *Geophysical Journal International*, **200**, 111–115.
- Wu, R. S., 1994. Wide-angle elastic wave one-way propagation in heterogeneous media and an elastic wave complex-screen method, *Journal of Geophysical Research*, **99**, 751–766.
- Xiao, X. & Leaney, W.S., 2010. Local vertical seismic profiling (VSP) elastic reverse-time migration and migration resolution: salt-flank imaging with transmitted P-to-S waves, *Geophysics*, **75**, S35–S49.
- Xie, X.B. & Wu, R.S., 2005. Multicomponent prestack depth migration using the elastic screen method, *Geophysics*, **70**, S30–S37.
- Yan, J. & Sava, P., 2008. Isotropic angle-domain elastic reverse-time migration, *Geophysics*, **73**, S229–S239.
- Yan, R. & Xie, X., 2012. An angle-domain imaging condition for elastic reverse time migration and its application to angle gather extraction, *Geophysics*, **77**, S105–S115.
- Yong, P., Huang, J., Li, Z., Liao, W., Qu, L., Li, Q. & Yuan, M., 2016. Elastic-wave reverse-time migration based on decoupled elastic-wave equations and inner-product imaging condition, *Journal of Geophysics and Engineering*, **13**, 953–963.
- Zhang, Q. & McMechan, G.A., 2010. 2D and 3D elastic wavefield vector decomposition in the wavenumber domain for VTI media, *Geophysics*, **75**, D13–D26.
- Zhang, Q. & McMechan, G.A., 2011. Direct vector-field method to obtain angle-domain common-image gathers from isotropic acoustic and elastic reverse time migration, *Geophysics*, **76**, WB135–WB149.